Mechanics of Materials 8 (1990) 269–283
Elsevier



# DEVELOPMENT OF A TEST METHOD FOR MEASURING THE MIXED MODE FRACTURE RESISTANCE OF BIMATERIAL INTERFACES

P.G. CHARALAMBIDES, H.C. CAO, J. LUND and A.G. EVANS

*Materials Department, College of Engineering, University of California, Santa Barbara, CA 93106, U.S.A.*

Received 2 March 1989; revised 22 May 1989

Measurements of the mixed mode fracture resistance of bimaterial interface have been shown to be appreciably influenced by the presence of loading point friction and by residual strain. Analyses of the effect of these phenomena on the strain energy release rate and on the phase angle of loading are presented. The analyses are used to interpret experimental measurements obtained on several bimaterial models.

## 1. Introduction

A test specimen for determining the mixed mode fracture resistance of bimaterial interfaces has been proposed (Charalambides et al., 1989). The specimen consists of a bimaterial beam tested in four-point flexure (Fig. 1). Analysis of this specimen (Charalambides et al., 1989) has been demonstrated that a steady-state regime obtains when the interface cracks reside between the inner loading lines. The corresponding phase angle of loading is of order $\pi/4$. The method thus samples the interface fracture resistance at a phase angle having importance to such problems as thin film decohesion (Drory et al., 1989) and fiber debonding in composites (Charalambides and Evans, 1989). Subsequent to the initial analysis of the specimen, a comprehensive test program has been conducted (Cao, 1988; Cao and Evans 1989; Lund, 1988; Reimanis et al., 1989) as needed to fully calibrate the specimen and to identify relevant testing issues. The measurements have, in turn, highlighted additional aspects of the test that require further analysis. The results of the analyses are described in this article, in conjunction with some typical data. The two most important experimental aspects of the test method not elucidated in the initial analysis concern the effects of friction at the loading points and of residual strain caused by thermal expansion mismatch. An experimental measurement of particular relevance

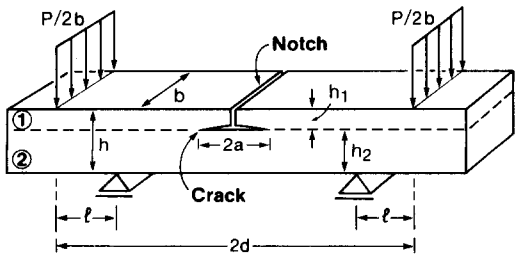


Fig. 1. Bimaterial notched four-point bending specimen with symmetrical interfacial cracks.

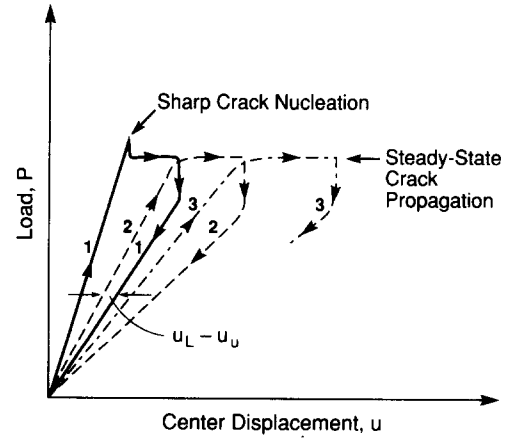


Fig. 2. A typical experimental load–displacement curve showing three loading/unloading cycles at three different crack lengths.

to the interpretation of friction concerns the hysteresis in the compliance obtained upon loading and unloading following crack extension (Fig. 2) (Lund, 1988). Analysis of these phenomena will be presented first and then used to rationalize the experimental results.

## 2. Near tip interface mechanics

In general, the complex stress intensity factor $K$ can be expressed in terms of its real Re and imaginary Im parts and/or its modulus $|K|$ and phase angle $\Psi$,

$$K = \mathrm{Re}(K) + \mathrm{i}\,\mathrm{Im}(K) \equiv |K|\,\mathrm{e}^{\mathrm{i}\Psi} \tag{1}$$

As discussed elsewhere (Charalambides et al., 1989; Rice, 1988), the bimaterial stress intensity factor and phase angle $\Psi$ are scale sensitive; an issue more thoroughly addressed by Rice (1988). Consequently, it is more convenient for comparison between materials to represent the interface fracture resistance locus in terms of trends in critical energy release rate $\mathcal{G}_c$, which is scale insensitive, with phase angle $\Psi$, where $\mathcal{G}$ is related to $K$ by

$$\mathcal{G} = \frac{\dfrac{1-\nu_1}{G_1} + \dfrac{1-\nu_2}{G_2}}{4\cosh^2(\pi\epsilon)} K\bar{K} \tag{2}$$

$$\epsilon = \frac{1}{2\pi} \ln \frac{1-\beta}{1+\beta}$$

where

$$\beta = \frac{1}{2}\left(\frac{G_1}{G_2}(1-2\nu_2) - (1-2\nu_1)\right) \times \Big/\left(\frac{G_1}{G_2}(1-\nu_2) + (1-\nu_1)\right)$$

is one of the plane strain Dundurs' parameters (Dundurs, 1968), and $G_i$ and $\nu_i$ $(i = 1, 2)$ are the shear modulus and Poisson's ratio for material 1 and 2, respectively. While it is important to use $\Psi$ to describe fracture data, it is convenient to present *calculated* phase angles using a scale invariant form

$$Kh^{\mathrm{i}\epsilon} = |K|\,\mathrm{e}^{\mathrm{i}\Psi^*} \tag{3}$$

where

$$\Psi^* = \Psi + \epsilon \ln h$$

with $h$ being a characteristic dimension: in this case, the beam thickness (Fig. 1).

## 3. Analysis of frictional effects

A schematic of the specimen with friction present is shown in Fig. 3. Assuming that Coulomb friction exists at the loading points, the friction load $F$ is related to the applied load $P$ through a friction coefficient $\mu$: $F = \mu P/2$. The overall elastic behavior is then obtained by superposition of the solutions for the applied and friction loads.

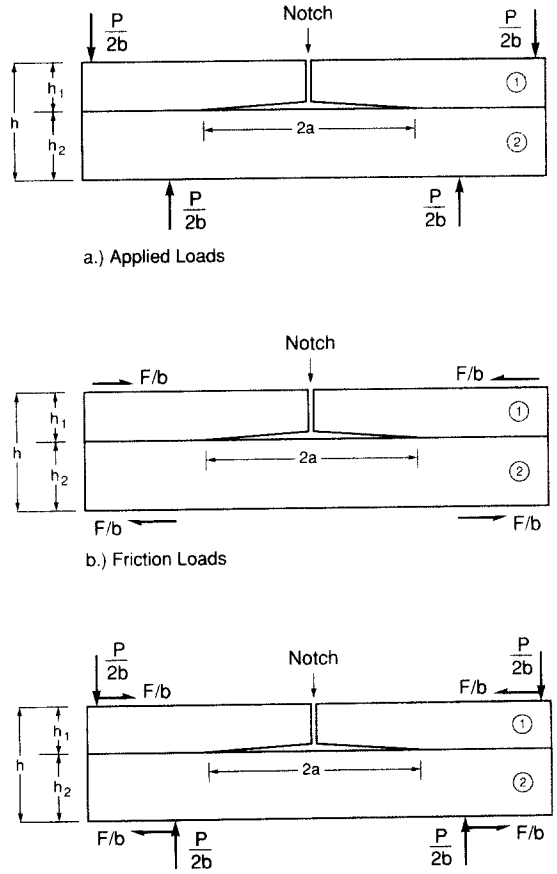


Fig. 3. A schematic of the loading conditions for the notched four-point bending specimen with symmetrical interfacial cracks.

Solutions for the energy release rate, phase angle and mid-point displacement caused by the applied load [1] have been presented elsewhere (Charalambides et al., 1989). In this section, the corresponding frictional effects are derived.

### 3.1 Energy release rates

The energy release and stress intensity factor acquire steady-state for interface cracks in the constant moment region (Charalambides et al., 1989), whereupon accurate steady-state energy release rates can be obtained analytically. In particular, the steady state $\mathcal{G}_{ss}$, is related to the strain energies in sections ('i) and (ii) (Charalambides and Evans, 1989; Charalambides et al., 1989) of the composite beam (Fig. 4), such that,

$$\mathcal{G}_{ss} = (1-\nu_2^2)\frac{M^2}{2E_2}\left[\frac{1}{I_2} - \frac{\lambda}{I_c}\right] \tag{4}$$

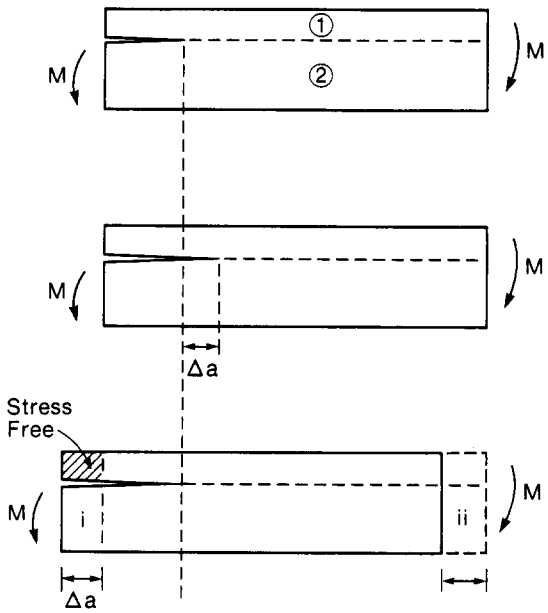


Fig. 4. A schematic representation of a virtual crack extension. The strain energy densities in regions i and ii were used to calculate the associated steady-state energy release rate $\mathcal{G}_{ss}$.

[1] Henceforth, the superscripts $()^P$ and $()^F$ will be used to refer to quantities associated with applied and friction loads, respectively.

where $M$ is the net bending moment per unit width, $I_2$ and $I_c$ are the second moments of inertia per unit cross-sectional area for the bottom layer and the composite beam, respectively, and $\lambda = (1-\nu_1^2)E_2/(1-\nu_2^2)E_1$ for plane strain. The moments governed by the applied and friction loads are $M^P = Pl/2b$ and $M^F = -Fh/b$, respectively, with $h$ being the total height of the beam and $l$ the spacing between the inner and outer loading lines (Fig. 1). Consequently, for Coulomb friction

$$M = M^P + M^F \equiv \frac{Pl}{2b}(1-\mu h/l) \tag{5}$$

and the steady state energy release rate becomes,

$$\frac{\mathcal{G}_{ss}E_2b^2h^3}{(1-\nu_2^2)P^2l^2} = \frac{3}{2}\left[\frac{1}{\eta_2^3} - \frac{\lambda}{\eta_1^3 + \lambda\eta_2^3 + 3\lambda\dfrac{\eta_1\eta_2}{\eta_1+\lambda\eta_2}}\right]\left(1-\mu\frac{h}{l}\right)^2 \equiv k_1(1-\mu h/l)^2 \tag{6}$$

where $\eta_i = h_i/h (i = 1, 2)$ and $k_1$ is given in Tables 1–4. The trends in $\mathcal{G}_{ss}$ with the height to spacing ratio $h/l$ for various friction coefficients $\mu$ are shown in Fig. 5. Evidently, the normalized $\mathcal{G}_{ss}$ decreases with increasing values of $\mu$ and $h/l$. Consequently, in order to minimize uncertainties associated with unknown frictional effects, relatively small $h/l$ should be used. Values in the interval $0.25 \leqslant (h/l) \leqslant 0.5$ seem practical. It is also apparent that neglect of friction, when it exists, would result in an overestimate of $\mathcal{G}_{ss}$.

Numerical methods give value for $\mathcal{G}$ both in steady-state and when the cracks are between the inner and outer load lines. For this purpose, finite element procedures have been applied (Fig. 6), using 8-noded plane strain isoparametric elements with four stations for the integration of the element stiffness. The total number of elements varied with the crack length $a/l$ and height ratio $h_1/h_2$. A focused mesh was used to discritize the near tip region (Fig. 6) and thus assure high accuracy (Charalambides and Evans, 1989; Matos et al.,

Table 1
The coefficients $c_i$, $i=1, 4$, $k_i$, $i=1, 3$ and $u_i$, $i=1, 2$ as a function of the crack length for modulus ratio $E_2/E_1=1.0$ and Poisson's ratio $\nu_1=\nu_2=0.3$

| $a/l$ | $c_1$ | $c_2$ | $c_3$ | $c_4$ | $k_1$ | $k_2$ | $k_3$ | $u_1$ | $u_2$ |
|---|---|---|---|---|---|---|---|---|---|
| 0.09 | 2.45 | −4.90 | 2.05 | −4.10 | 10.21 | −40.84 | 40.84 | 6.39 | −12.44 |
| 0.16 | 2.45 | −4.90 | 2.11 | −4.21 | 10.43 | −41.73 | 41.73 | 7.37 | −14.41 |
| 0.31 | 2.45 | −4.90 | 2.12 | −4.24 | 10.49 | −41.96 | 41.96 | 9.88 | −19.43 |
| 0.47 | 2.45 | −4.90 | 2.12 | −4.24 | 10.49 | −41.97 | 41.97 | 12.40 | −24.48 |
| 0.63 | 2.45 | −4.90 | 2.12 | −4.24 | 10.49 | −41.99 | 41.99 | 14.95 | −29.58 |
| 0.78 | 2.45 | −4.90 | 2.12 | −4.24 | 10.51 | −42.02 | 42.00 | 17.52 | −34.72 |
| 0.94 | 2.46 | −4.89 | 2.12 | −4.24 | 10.56 | −42.04 | 41.85 | 20.12 | −39.90 |
| 1.09 | 2.47 | −4.80 | 2.12 | −4.23 | 10.62 | −41.71 | 40.98 | 22.75 | −45.09 |
| 1.25 | 2.45 | −4.51 | 2.12 | −4.19 | 10.50 | −39.90 | 37.94 | 25.40 | −50.16 |
| 1.41 | 2.25 | −3.96 | 2.09 | −3.98 | 9.43 | −34.46 | 31.52 | 27.99 | −54.86 |
| 1.5 | Inner loading line | | | | | | | | |
| 1.56 | 1.84 | −3.64 | 1.87 | −3.62 | 6.87 | −26.92 | 26.37 | 30.27 | −59.07 |
| 1.72 | 1.42 | −3.65 | 1.53 | −3.53 | 4.35 | −21.15 | 25.77 | 32.11 | −63.14 |
| 1.88 | 1.05 | −3.67 | 1.19 | −3.53 | 2.51 | −16.05 | 25.91 | 33.51 | −67.25 |
| 2.03 | 0.67 | −3.72 | 0.86 | −3.53 | 1.19 | −11.06 | 26.28 | 34.50 | −71.42 |
| 2.19 | 0.29 | −3.91 | 0.52 | −3.51 | 0.36 | −5.94 | 27.60 | 35.07 | −75.72 |
| 2.5 | Outer loading line | | | | | | | | |

1989). The results can be expressed in the non-dimensional form,

$$\frac{\mathcal{G}E_2b^2h^3}{(1-\nu_2^2)P^2l^2}=k_1+k_2\frac{\mu h}{2l}+k_3\left(\frac{\mu h}{2l}\right)^2 \qquad (7)$$

where $k_i$ ($i=1$–$3$) are summarized in Tables 1–4. The trends in $\mathcal{G}$ with $a/l$ and coefficient of friction in the interval $0\leqslant\mu\leqslant 0.5$ are also plotted on Fig. 7.

Table 2
The coefficients $c_i$, $i=1, 4$, $k_i$, $i=1, 3$ and $u_i$, $i=1, 2$ as a function of the crack length for modulus ratio $E_2/E_1=2.5$ and Poisson's ratios $\nu_1=\nu_2=0.3$

| $a/l$ | $c_1$ | $c_2$ | $c_3$ | $c_4$ | $k_1$ | $k_2$ | $k_3$ | $u_1$ | $u_2$ |
|---|---|---|---|---|---|---|---|---|---|
| 0.09 | 1.69 | −3.38 | 1.59 | −3.18 | 9.29 | −37.15 | 37.15 | 8.38 | −16.30 |
| 0.16 | 1.68 | −3.35 | 1.63 | −3.27 | 9.45 | −37.80 | 37.80 | 9.30 | −18.15 |
| 0.31 | 1.68 | −3.35 | 1.65 | −3.29 | 9.51 | −38.03 | 38.03 | 11.66 | −22.86 |
| 0.47 | 1.68 | −3.35 | 1.65 | −3.29 | 9.51 | −38.04 | 38.04 | 14.05 | −27.64 |
| 0.63 | 1.68 | −3.35 | 1.65 | −3.29 | 9.51 | −38.04 | 38.02 | 16.47 | −32.49 |
| 0.78 | 1.68 | −3.35 | 1.65 | −3.29 | 9.52 | −38.01 | 37.94 | 18.94 | −37.41 |
| 0.94 | 1.68 | −3.32 | 1.65 | −3.28 | 9.53 | −37.85 | 37.59 | 21.43 | −42.38 |
| 1.09 | 1.67 | −3.25 | 1.64 | −3.25 | 9.48 | −37.17 | 36.43 | 23.97 | −47.36 |
| 1.25 | 1.63 | −3.04 | 1.63 | −3.18 | 9.17 | −34.97 | 33.37 | 26.51 | −52.22 |
| 1.41 | 1.47 | −2.69 | 1.57 | −2.98 | 7.96 | −29.75 | 27.80 | 28.95 | −56.72 |
| 1.5 | Inner loading line | | | | | | | | |
| 1.56 | 1.18 | −2.52 | 1.37 | −2.73 | 5.64 | −23.17 | 23.80 | 31.06 | −60.80 |
| 1.72 | 0.90 | −2.53 | 1.10 | −2.68 | 3.50 | −18.08 | 23.43 | 32.72 | −64.83 |
| 1.88 | 0.65 | −2.55 | 0.84 | −2.69 | 1.96 | −13.54 | 23.63 | 33.97 | −68.93 |
| 2.03 | 0.41 | −2.60 | 0.59 | −2.71 | 0.89 | −9.19 | 24.36 | 34.82 | −73.13 |
| 2.5 | Outer loading line | | | | | | | | |

Table 3
The coefficients $c_i$, $i=1, 4$, $k_i$, $i=1, 3$ and $u_i$, $i=1, 2$ as a function of the crack length for modulus ratio $E_2/E_1=10$ and Poisson's ratios $\nu_1=\nu_2=0.3$

| $a/l$ | $c_1$ | $c_2$ | $c_3$ | $c_4$ | $k_1$ | $k_2$ | $k_3$ | $u_1$ | $u_2$ |
|---|---|---|---|---|---|---|---|---|---|
| 0.09 | 0.78 | −1.57 | 0.79 | −1.57 | 6.40 | −25.62 | 25.61 | 13.54 | −26.09 |
| 0.16 | 0.77 | −1.54 | 0.81 | −1.61 | 6.47 | −25.88 | 25.88 | 14.26 | −27.55 |
| 0.31 | 0.77 | −1.54 | 0.81 | −1.63 | 6.51 | −26.03 | 26.02 | 16.15 | −31.32 |
| 0.47 | 0.77 | −1.53 | 0.81 | −1.62 | 6.50 | −25.98 | 25.96 | 18.11 | −35.24 |
| 0.63 | 0.77 | −1.53 | 0.18 | −1.62 | 6.48 | −25.87 | 25.84 | 20.14 | −39.30 |
| 0.78 | 0.76 | −1.52 | 0.81 | −1.61 | 6.43 | −25.64 | 25.57 | 22.25 | −43.50 |
| 0.94 | 0.76 | −1.50 | 0.80 | −1.60 | 6.33 | −25.16 | 25.01 | 24.41 | −47.81 |
| 1.09 | 0.74 | −1.45 | 0.79 | −1.57 | 6.11 | −24.13 | 23.84 | 26.62 | −52.17 |
| 1.25 | 0.70 | −1.36 | 0.77 | −1.52 | 5.62 | −22.06 | 21.65 | 28.82 | −56.46 |
| 1.41 | 0.61 | −1.24 | 0.71 | −1.42 | 4.60 | −18.43 | 18.46 | 30.88 | −60.49 |
| 1.5 | Innerloading line | | | | | | | | |
| 1.56 | 0.48 | −1.19 | 0.61 | −1.33 | 3.11 | −14.35 | 16.60 | 32.59 | −64.34 |
| 1.72 | 0.36 | −1.21 | 0.48 | −1.33 | 1.85 | −11.11 | 16.86 | 33.90 | −68.32 |
| 1.88 | 0.25 | −1.26 | 0.35 | −1.36 | 0.97 | −8.26 | 17.88 | 34.84 | −72.55 |
| 2.03 | 0.15 | −1.37 | 0.23 | −1.44 | 0.39 | −5.56 | 20.57 | 35.45 | −77.19 |
| 2.5 | Outer loading line | | | | | | | | |

### 3.2. Phase angles

The non-dimensional phase angles $\Psi^*$ can be calculated using the finite element procedure described above. The results have the non-dimensional form,

$$\Psi^* \equiv \arctan \frac{\mathrm{Im}(Kh^{i\epsilon})}{\mathrm{Re}(Kh^{i\epsilon})} = \arctan \frac{c_3 + c_4(\mu h/2l)}{c_1 + c_2(\mu h/2l)} \tag{8}$$

where the coefficients $c_1$, $c_3$ are due to $P$ and $c_2$, $c_4$ due to $F$. The values obtained for these coefficients with respect to crack length $a/l$ and modulus ratio $E_2/E_1$ (for Poisson's ration $\nu_1=\nu_2=0.3$ and $h_1=h_2$) are summarized in Table 1–4. As expected, friction has no effect on the phase angle for cracks in the constant moment region. On the contrary, as the crack enters the transient zone between the inner and outer loading lines, the phase angle becomes sensitive to crack length and increases substantially with increase in friction

Table 4
The coefficients $c_i$, $i=1, 4$, $k_i$, $i=1, 3$ and $u_i$, $i=1, 2$ as a function of the crack length for modulus ratio $E_2/E_1=25$ and Poisson's ratios $\nu_1=\nu_2=0.3$

| $a/l$ | $c_1$ | $c_2$ | $c_3$ | $c_4$ | $k_1$ | $k_2$ | $k_3$ | $u_1$ | $u_2$ |
|---|---|---|---|---|---|---|---|---|---|
| 0.31 | 0.40 | −0.79 | 0.42 | −0.84 | 3.98 | −15.94 | 15.94 | 19.56 | −37.22 |
| 0.63 | 0.39 | −0.78 | 0.41 | −0.83 | 3.93 | −15.74 | 15.76 | 22.87 | −43.85 |
| 0.94 | 0.38 | −0.76 | 0.41 | −0.82 | 3.75 | −15.09 | 15.16 | 26.56 | −51.25 |
| 1.25 | 0.34 | −0.70 | 0.38 | −0.78 | 3.17 | −12.99 | 13.30 | 30.43 | −59.11 |
| 1.41 | 0.30 | −0.66 | 0.35 | −0.74 | 2.52 | −10.89 | 11.80 | 32.23 | −62.95 |
| 1.5 | Inner loading line | | | | | | | | |
| 1.56 | 0.23 | −0.65 | 0.29 | −0.71 | 1.65 | −8.62 | 11.30 | 33.69 | −66.81 |
| 1.72 | 0.17 | −0.70 | 0.22 | −0.73 | 0.95 | −6.80 | 12.37 | 34.79 | −71.09 |
| 1.88 | 0.11 | −0.77 | 0.16 | −0.79 | 0.47 | −5.20 | 14.77 | 35.54 | −76.00 |
| 2.03 | 0.06 | −0.93 | 0.09 | −0.91 | 0.16 | −3.55 | 20.46 | 36.01 | −82.01 |
| 2.5 | Outer loading line | | | | | | | | |

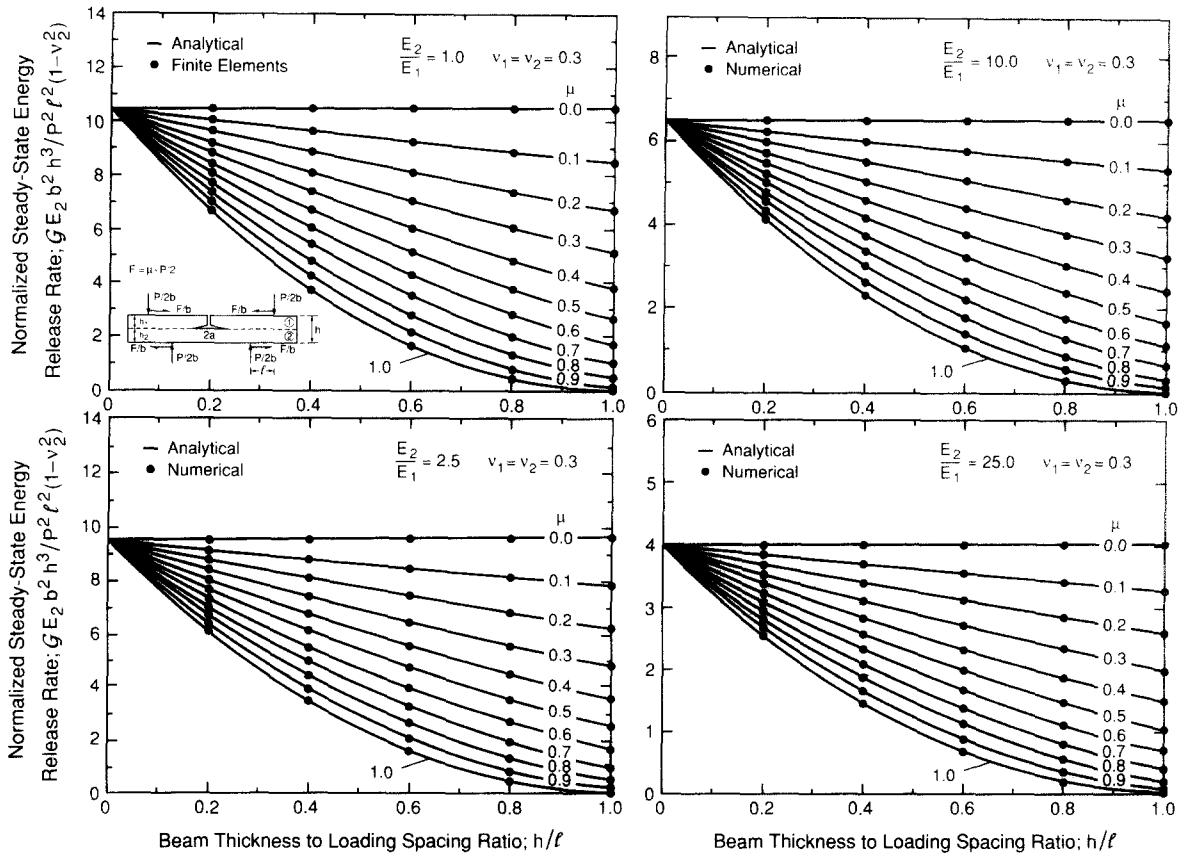


Fig. 5. The trends in normalized steady-state energy release rate $\mathcal{G}_{ss}$ with the height to spacing ratio $h/l$ for various friction coefficient $\mu$ and elastic modulus ratios $E_2/E$.

coefficient. Such effects for various modulus ratios and friction coefficients in the interval $0 \leqslant \mu \leqslant 0.5$ are shown in Fig. 8.

### 3.3 Beam compliances

Numerical estimates of the mid-point deflection of the composite beam were also obtained using the finite element analysis. Calculated trends in the normalized mid-point deflections $u^P$ and $u^F$ caused by the applied and frictional loads, respectively, have the form,

$$u^P = \frac{u_1 Pld^2}{E_2 bh^3}$$

and

$$u^F = \frac{u_2 Fhd^2}{E_2 bh^3}$$

with $u_i (i = 1, 2)$ being the coefficients summarized in Tables 1–4 and $2d$ is the spacing between the outer loading lines. Then, linear superposition dictates that the total mid-point beam deflection during *loading* be

$$u_L \equiv u^P + u^F = [u_1 + u_2 \mu h/2l] \frac{Pld^2}{E_2 bh^3} \tag{9a}$$

whereas, on *unloading* because of the reversal of friction

$$u_u \equiv u^P - u^F = [u_1 - u_2 \mu h/2l] \frac{Pld^2}{E_2 bh^3} \tag{9b}$$

The trends in compliance, $u^P$ with crack length, for $h/l = 0.5$, and coefficients of friction in the interval $0 \leqslant \mu \leqslant 0.5$ are shown in Fig. 9. The in-

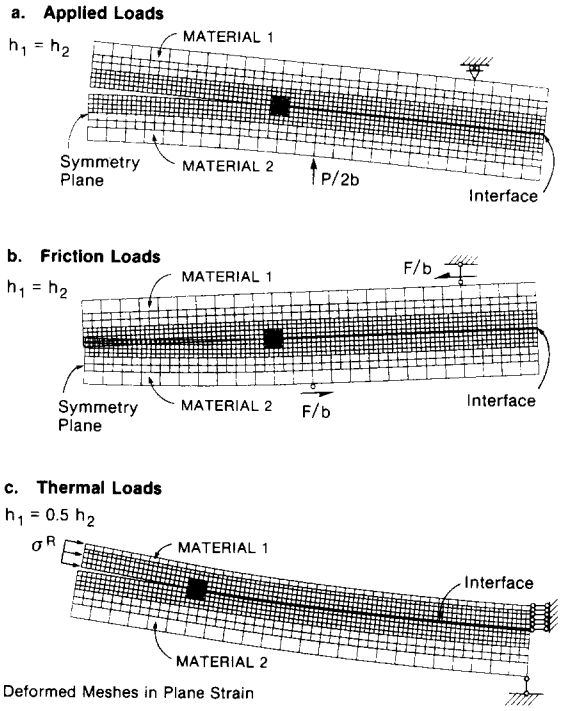


Fig. 6. Deformed finite element meshes.

fluence of friction is evidently substantial. These compliances can, in fact, be used to extract the operative friction coefficients for any test system by noting that,

$$\mu = 2(u_1/u_2)(l/h)(u_L - u_u)/(u_L + u_u) \qquad (10)$$

Consequently, by knowing the crack length to obtain $u_1$ and $u_2$ and by measuring the loading and unloading compliances without crack growth, $\mu$ can be deduced, as elaborated above.

## 4. Analysis of residual stress effects

### *4.1 Energy release rates*

Using standard procedures (Fig. 10), the thermal loading can be replaced by an axial force $N^R$ [2] and a bending moment $M^R$. For this case, steady-state conditions obtain throughout, provided that $a/h_s \geq 4$, where $h_s = \min(h_1, h_2)$. In the presence of both the applied moment $M^P$ and the thermal loads $N^R$ and $M^R$, the net steady-state energy release rate is obtained as the difference of the strain energies in sectors i and ii shown in Fig. 4. The result can be expressed in the form

$$\mathcal{G}_{SS}^T = \mathcal{G}^R + \mathcal{G}^{RP} + \mathcal{G}^P \qquad (11)$$

where $\mathcal{G}^R$ and $\mathcal{G}^P$ are the decoupled energy release rates generated by the thermal and applied loads respectively and $\mathcal{G}^{RP}$ represents their interaction. The individual terms are given by;

$$\mathcal{G}^R = \frac{1-\nu_1^2}{2E_1}\left[\left(\frac{1}{A_1} - \frac{1}{A_c}\right)(N^R)^2 - \frac{(M^R)^2}{I_c}\right]$$

$$\mathcal{G}^P = \frac{(1-\nu_1^2)(M^P)^2}{2E_1}\left[\frac{1}{\lambda I_2} - \frac{1}{I_c}\right]$$

$$\mathcal{G}^{RP} = \frac{(1-\nu_1^2)M^R M^P}{E_1 I_c}$$

where $A_1$ and $A_c$ are the cross-sectional areas per unit width of the top layer and the composite beam, respectively. The loads and moments can be expressed in terms of stresses such that,

$$N^R = h_1 \sigma^R$$

$$M^R = \frac{h_1^2}{2}\left[\frac{\lambda\eta(1+\eta)}{1+\lambda\eta}\right]\sigma^R$$

$$M^P = \frac{h_2^2}{6}\sigma^P \qquad (12)$$

where for plane strain, the mismatch stress is

$$\sigma^R = \frac{E_1(\alpha_2 - \alpha_1)\,\Delta T}{(1-\nu_1)}$$

with $\alpha_i$ $(i = 1, 2)$ being the thermal expansion coefficient for the layer $i$, $\Delta T = T_{final} - T_{initial}$ being the temperature difference, $\eta = h_2/h_1$, and $\sigma^P$ is the maximum tensile bending stress due to $M^P$ applied at the bottom layer alone.

Consequently, the energy release rate components can be presented in non-dimensional form as

$$\frac{\mathcal{G}^R E_2 b^2 h^3}{P^2 l^2 (1-\nu_2^2)}$$

[2] The superscript $(\,)^R$ refers to the thermal load.

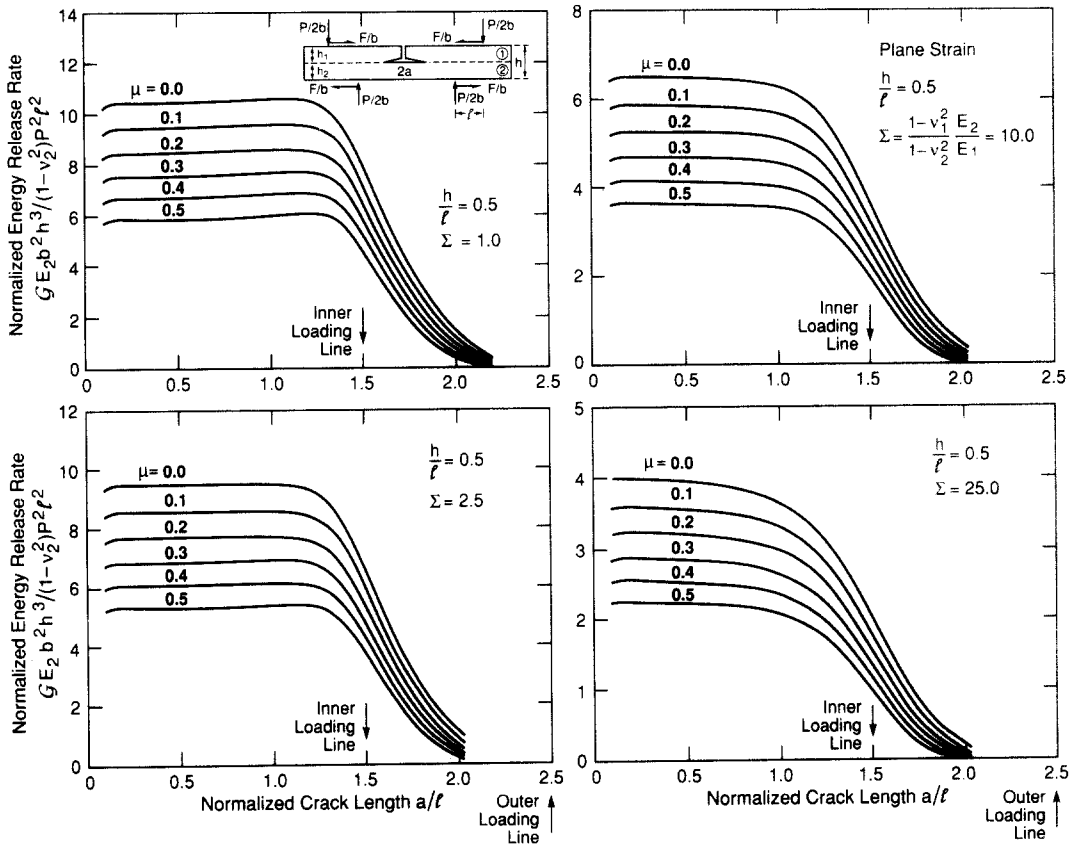


Fig. 7. The trends in normalized energy release rate $\mathcal{G}$ with crack length for various friction coefficients and elastic modulus ratios. These results were obtained for $h/l = 0.5$ and Poisson's ratios $\nu_1 = \nu_2 = 0.3$.

$$= \tfrac{9}{2}\lambda^2\left(\frac{1+\eta}{\eta}\right)^3\left\{\frac{1}{1+\lambda\eta} - \frac{3}{1+\lambda\eta^3+3\lambda\eta\dfrac{(1+\eta)^2}{1+\lambda\eta}}\left(\frac{1+\eta}{1+\lambda\eta}\right)^2\right\} \times \left(\sigma^R/\sigma^P\right)^2$$

$$\frac{\mathcal{G}^{RP}E_2b^2h^3}{P^2l^2\left(1-\nu_2^2\right)} = \frac{9\lambda^2}{1+\lambda\eta^3+3\lambda\eta\dfrac{(1+\eta)^2}{1+\lambda\eta}}\frac{(1+\eta)^4}{\eta(1+\lambda\eta)}\left(\sigma^R/\sigma^P\right)$$

$$\frac{\mathcal{G}^{P}E_2b^2h^3}{P^2l^2\left(1-\nu_2^2\right)} = \frac{3}{2}\left\{\frac{1}{\eta^3} - \frac{\lambda}{1+\lambda\eta^3+3\lambda\eta\dfrac{(1+\eta)^2}{1+\lambda\eta}}\right\}(1+\eta)^3 \tag{13}$$

such that,

$$\frac{\mathcal{G}_{SS}E_2b^2h^3}{P^2l^2\left(1-\nu_2^2\right)} = g_1 + g_2\tau + g_3\tau^2 \tag{14}$$

where $\tau$ is the ratio between the thermal and applied stresses, $\sigma^R/\sigma^P$. The trends in $g_1$ with $h_1/h_2$ and $E_2/E_1$ can be found in a previous

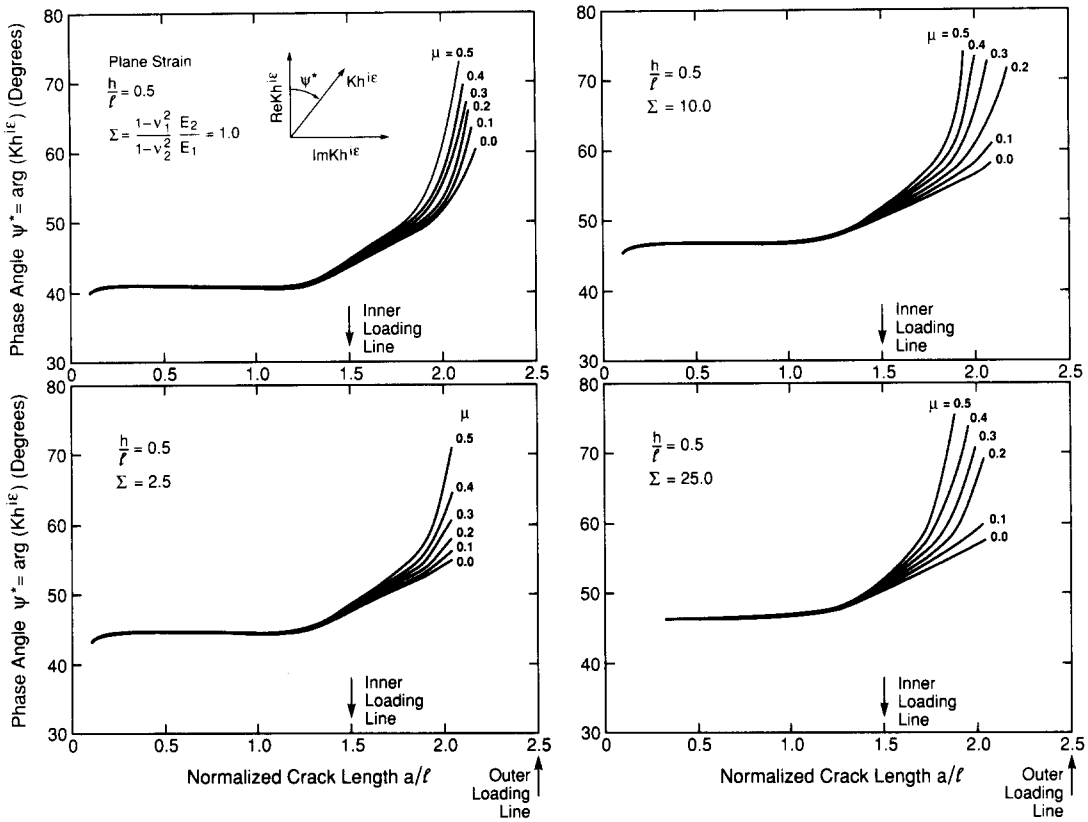


Fig. 8. The trends in the non-dimensional phase angle $\Psi^*$ due to applied and friction loads with crack length for various friction coefficients and elastic modulus ratios.

article (Charalambides et al., 1989). The corresponding trends in $g_3$ due to thermal loads alone are shown in Fig. 11 and Tables 5–8. For large $h_2/h_1$ ($\geqslant 60$), the results correspond to those for thin films and are in agreement with solutions reported elsewhere (Drory et al., 1989; Suo and Hutchinson, 1989). Results for combined loads (Fig. 12) in the range where combined effects are prevalent, $-2\sigma^R/\sigma^P < 2$, emphasize an important asymmetry. Specifically, for a system with $\Delta T < 0$

Table 5
The coefficients $c_i$, $i = 5$, 8 and $g_i$, $i = 1$, 3 for the modulus ratio $E_2/E_1 = 1.0$ and Poisson's ratios $\nu_1 = \nu_2 = 0.3$

| $h_1/h_2$ | $c_5$ | $c_6$ | $c_7$ | $c_8$ | $g_1$ | $g_2$ | $g_3$ |
|---|---|---|---|---|---|---|---|
| 0.10 | 0.46 | 0.41 | 0.51 | 0.47 | 0.50 | 0.90 | 0.41 |
| 0.20 | 0.72 | 0.50 | 0.75 | 0.71 | 1.09 | 1.80 | 0.76 |
| 0.30 | 0.95 | 0.54 | 0.94 | 0.88 | 1.80 | 2.70 | 1.07 |
| 0.40 | 1.16 | 0.54 | 1.12 | 1.04 | 2.62 | 3.60 | 1.37 |
| 0.50 | 1.38 | 0.51 | 1.28 | 1.19 | 3.56 | 4.50 | 1.69 |
| 0.60 | 1.59 | 0.45 | 1.45 | 1.36 | 4.64 | 5.40 | 2.05 |
| 0.70 | 1.80 | 0.36 | 1.61 | 1.53 | 5.87 | 6.30 | 2.49 |
| 0.80 | 2.02 | 0.26 | 1.77 | 1.72 | 7.23 | 7.20 | 3.02 |
| 0.90 | 2.24 | 0.14 | 1.94 | 1.91 | 8.79 | 8.10 | 3.66 |
| 1.00 | 2.45 | 0.00 | 2.12 | 2.12 | 10.50 | 9.00 | 4.50 |

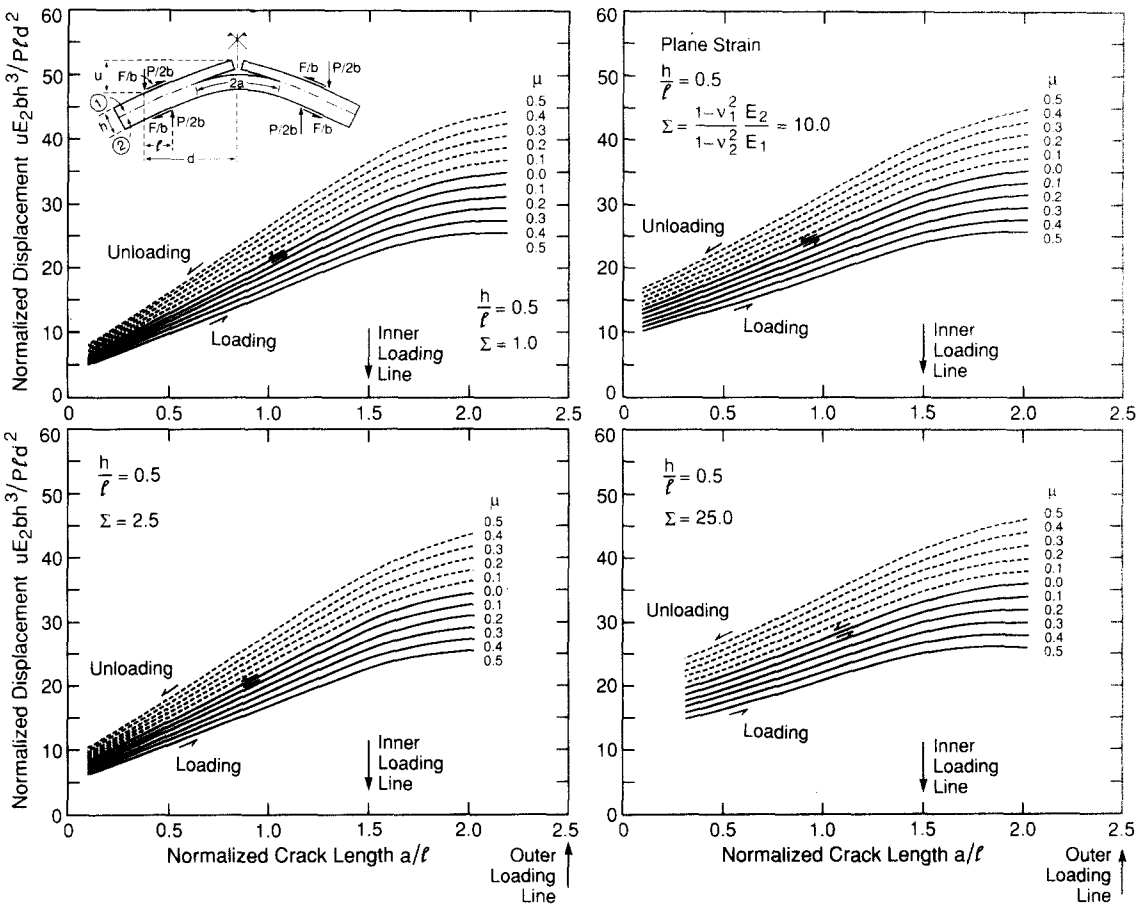


Fig. 9. Loading and unloading compliances as a function of crack length for various friction coefficients. These results were obtained for $h/l = 0.5$ and Poisson's ratios $\nu_1 = \nu_2 = 0.3$.

and $\alpha_2 > \alpha_1$ (the *negative* axis in Fig. 12), $\mathcal{G}$ initially *decreases* as load is applied, because the residual compression in the film induces a diminished net strain as $\sigma^P$ increases. Consequently, crack extension is initially inhibited. Conversely, when $\alpha_1 > \alpha_2$, $\mathcal{G}$ systematically increases as the load is applied.

Table 6
The coefficients $c_i$, $i = 5$, 8 and $g_i$, $i = 1$, 3 for modulus ratio $E_2/E_1 = 2.5$ and Poisson's ratios $\nu_1 = \nu_2 = 0.3$

| $h_1/h_2$ | $c_5$ | $c_6$ | $c_7$ | $c_8$ | $g_1$ | $g_2$ | $g_3$ |
|---|---|---|---|---|---|---|---|
| 0.10 | 0.21 | 0.47 | 0.30 | 0.71 | 0.25 | 1.11 | 1.26 |
| 0.20 | 0.37 | 0.64 | 0.47 | 1.08 | 0.63 | 2.62 | 2.73 |
| 0.30 | 0.53 | 0.77 | 0.63 | 1.38 | 1.17 | 4.43 | 4.31 |
| 0.40 | 0.69 | 0.85 | 0.78 | 1.65 | 1.87 | 6.49 | 5.94 |
| 0.50 | 0.85 | 0.89 | 0.92 | 1.91 | 2.73 | 8.73 | 7.64 |
| 0.60 | 1.02 | 0.88 | 1.06 | 2.16 | 3.76 | 11.09 | 9.41 |
| 0.70 | 1.18 | 0.83 | 1.21 | 2.42 | 4.94 | 13.55 | 11.33 |
| 0.80 | 1.35 | 0.75 | 1.35 | 2.69 | 6.29 | 16.09 | 13.45 |
| 0.90 | 1.52 | 0.63 | 1.49 | 2.96 | 7.81 | 18.67 | 15.86 |
| 1.00 | 1.68 | 0.49 | 1.65 | 3.25 | 9.51 | 21.30 | 18.64 |

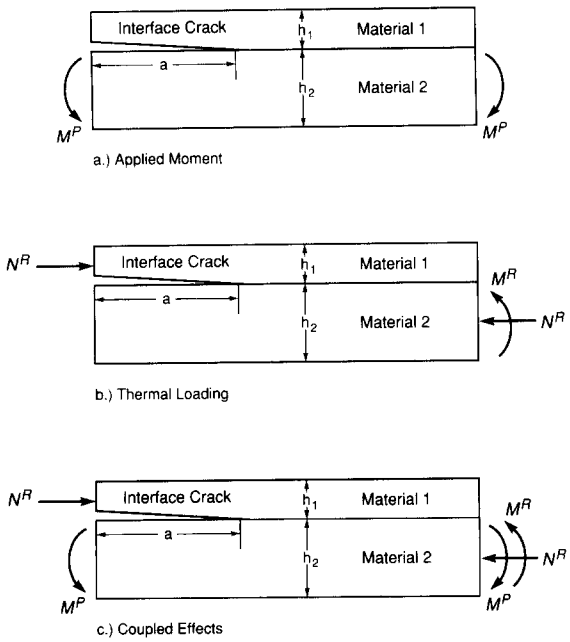


Fig. 10. A schematic of the loading conditions.

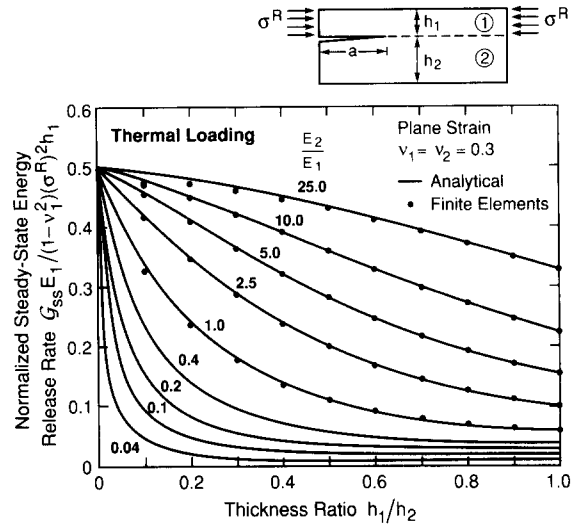


Fig. 11. Trends in normalized steady-state residual energy release rate $\mathcal{G}^R$ with relative thickness ratio $h_1/h_2$, for various modulus ratios $E_2/E_1$ with Poisson's ratios $\nu_1 = \nu_2 = 0.3$.

### 4.2 Stress intensities and phase angles

The stress intensities and the associated phase angle generated by the thermal residual stresses are calculated using finite elements. This thermal boundary value problem can be solved using Eshelby's procedure (cutting–straining–welding–relaxing), depicted together with the mesh used to obtain the finite element solutions on Fig. 6. The resulting stress intensity factor and phase angle are given by

$$(Kh^{i\epsilon})^R = (c_6 + ic_8)h_1^{1/2}\frac{\sigma^R}{\sigma^P}\frac{Pl}{bh^{3/2}}$$

$$(\Psi^*)^R = \arctan\frac{c_8}{c_6} \tag{15a}$$

where $c_i$ ($i = 5$–$8$) are given in Table 5–8. For the homogeneous case ($\lambda = 1$), the phase angle varies between the limiting thin film value of 52° to a value of 90° for a beam with equal layer thicknesses. However, $(\Psi^*)^R$ becomes less sensitive to

Table 7
The coefficients $c_i$, $i = 5$, 8 and $g_i$, $i = 1$, 3 for modulus ratio $E_2/E_1 = 10.0$ and Poisson's ratios $\nu_1 = \nu_2 = 0.3$

| $h_1/h_2$ | $c_5$ | $c_6$ | $c_7$ | $c_8$ | $g_1$ | $g_2$ | $g_3$ |
|---|---|---|---|---|---|---|---|
| 0.10 | 0.05 | 0.45 | 0.10 | 0.97 | 0.07 | 1.26 | 5.72 |
| 0.20 | 0.10 | 0.69 | 0.17 | 1.50 | 0.20 | 3.37 | 14.06 |
| 0.30 | 0.16 | 0.94 | 0.23 | 1.98 | 0.43 | 6.51 | 25.10 |
| 0.40 | 0.23 | 1.18 | 0.31 | 2.46 | 0.78 | 10.79 | 38.78 |
| 0.50 | 0.31 | 1.39 | 0.38 | 2.94 | 1.27 | 16.27 | 54.89 |
| 0.60 | 0.39 | 1.56 | 0.46 | 3.41 | 1.93 | 22.93 | 73.19 |
| 0.70 | 0.48 | 1.70 | 0.55 | 3.88 | 2.77 | 30.71 | 93.42 |
| 0.80 | 0.57 | 1.79 | 0.63 | 4.35 | 3.81 | 39.51 | 115.38 |
| 0.90 | 0.67 | 1.84 | 0.72 | 4.83 | 5.06 | 49.23 | 139.00 |
| 1.00 | 0.76 | 1.85 | 0.81 | 5.30 | 6.52 | 59.75 | 164.32 |

Table 8
The coefficients $c_i$, $i = 5$, 8 and $g_i$, $i = 1$, 3 for modulus ratio $E_2/E_1 = 25.0$ and Poisson's ratios $\nu_1 = \nu_2 = 0.3$

| $h_1/h_2$ | $c_5$ | $c_6$ | $c_7$ | $c_8$ | $g_1$ | $g_2$ | $g_3$ |
|---|---|---|---|---|---|---|---|
| 0.10 | 0.0 | 0.43 | 0.04 | 1.04 | 0.03 | 1.29 | 14.70 |
| 0.20 | 0.04 | 0.69 | 0.07 | 1.62 | 0.09 | 3.58 | 37.29 |
| 0.30 | 0.07 | 0.98 | 0.10 | 2.18 | 0.19 | 7.18 | 69.19 |
| 0.40 | 0.10 | 1.28 | 0.14 | 2.75 | 0.36 | 12.43 | 111.26 |
| 0.50 | 0.14 | 1.58 | 0.18 | 3.33 | 0.61 | 19.64 | 164.46 |
| 0.60 | 0.18 | 1.86 | 0.22 | 3.93 | 0.98 | 29.08 | 229.13 |
| 0.70 | 0.23 | 2.13 | 0.26 | 4.55 | 1.47 | 40.95 | 305.25 |
| 0.80 | 0.28 | 2.38 | 0.31 | 5.17 | 2.13 | 55.41 | 392.64 |
| 0.90 | 0.33 | 2.61 | 0.36 | 5.81 | 2.97 | 72.50 | 490.85 |
| 1.00 | 0.38 | 2.80 | 0.41 | 6.45 | 4.01 | 92.21 | 599.39 |

the thickness ratio as the modulus ratio $E_2/E_1$ increases.

The coupled effects of thermal and applied loadings on the phase angle have the general form,

$$\Psi^* = \arctan \frac{c_7 + c_8\tau}{c_5 + c_6\tau} \tag{15b}$$

Trends in $\Psi^*$ are plotted in Fig. 13. Generally, $\Psi^*$ is insensitive to geometry and loading, except when $\sigma^P$ is small. For small $\sigma^P$ and for cases wherein the residual stress is compressive, the phase angle changes sign as the beam is initially loaded, resulting in dramatic changes in $\Psi^*$. Consequently, when residual compressive stresses are

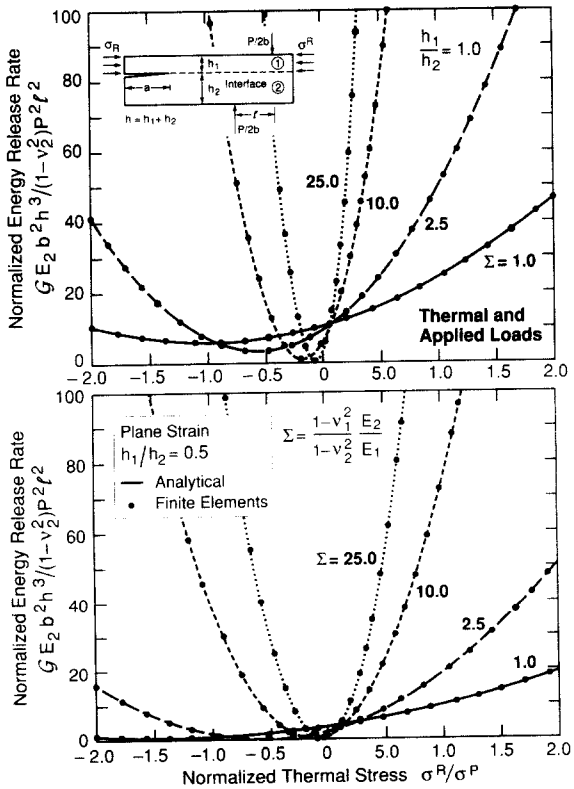


Fig. 12. The trends in normalized steady-state energy release rate due to applied and thermal loads, with the stress ratio $\sigma^R/\sigma^P$ for various moduli.

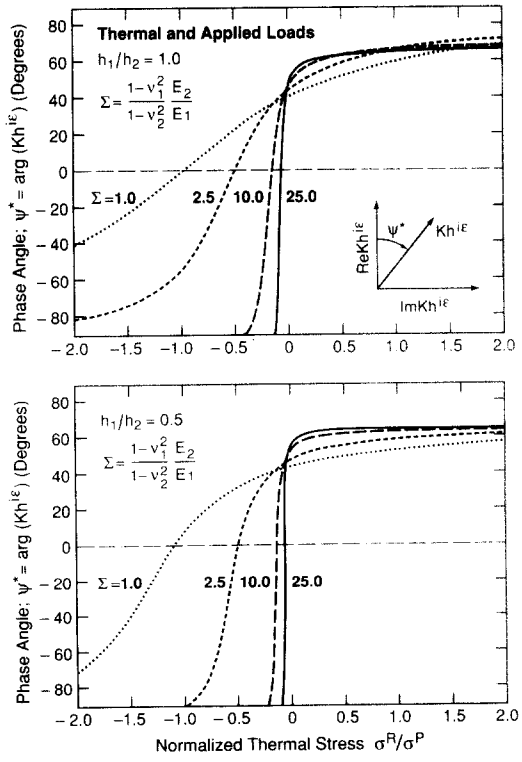


Fig. 13. The trends in non-dimensional phase angle $\Psi^*$ due to applied and thermal loads, with the stress ratio $\sigma^R/\sigma^P$ for various moduli.

present, crack extension may be subject to wide variations in phase angle.

## 5. Fracture resistance measurements

### 5.1 Procedure

The test materials used to validate the preceding analysis all involve bimaterials bonded with a thin ( ~ 25 μm) amorphous layer: either an organic polymer or an inorganic glass (Table 9). The details concerning specimen preparation are described elsewhere (Cao, 1988; Cao and Evans, 1989; Lund, 1988; Reimanis et al., 1989). The materials and bonding conditions have been selected in all but one case to avoid residual strain effects [3], as needed to systematically address the role of friction. Residual stresses are present in the Al/glass system (Table 9). The results obtained on this system allow investigation of the additional effects of mismatch stress, $\sigma^R$.

The incorporation of an interfacial precrack is achieved by loading the notched section in three-point flexure such that the crack, once initiated, propagates subject to diminishing $\mathcal{G}$ and thus arrests. In some cases, substantial overloads are needed to initiate the crack from the notch. In such instances, the arrest process is facilitated by subjecting the specimen to a compressive prestress at a predetermined crack arrest site (Lund, 1988), Specimens, one precracked, are subjected to four-point flexure and the center line displacements monitored. Initially, the loading and unloading compliances are measured (Fig. 2), as needed to assess the magnitude of the lateral tractions at the loading points, caused by friction. When the friction is excessive, test fixture modifications are made in order to reduce $\mu$ to a level that provides consistent values of the interface fracture resistance. Such modifications include changes in the test span, reduction of the surface roughness of the loading rods and of the specimen, incorporation of a solid lubricant between the specimen and the loading rods, etc. Following these modifications, the compliance hysteresis is remeasured and then the load slowly increased to the critical value for crack extension, as ascertained from the onset of a compliance increase.

Table 9
Bimaterial systems tested

| Materials | Bond layer | $\Psi$ (deg) | $\Psi_{tip}$ (deg) | $\mathcal{G}_c$ ($J_m^{-2}$) |
|---|---|---|---|---|
| PMMA/Al | Epoxy | 68 | 78 | 6 |
| Glass/Steel | Epoxy | 53 | 64 | 26 |
| Glass/Glass | Thermoplastic | 42 | 52 | 7 |
| $Al_2O_3/Al_2O_3$ | Glass | 42 | 36 | 10 |
| Al/Glass | Thermoplastic | 42 | 53 | 2 |

Note: To obtain the phase angle, $\Psi$, the units used for all dimensions were *micro-meters* (μm).

[3] The residual stress existing in the thin bond layer does not contribute to the mixed mode fracture resistance.

In the Al/glass system, the presence of residual stress was determined from the residual bending (Cao, 1988; Cao and Evans, 1989), giving a misfit stress of 10 MPa. This stress arose because bonding with the thermoplastic was conducted at ~ 100 °C and because the Al and glass have different thermal expansion coefficients.

### 5.2 The critical energy release rate

The first step in the analysis of the data involves determination of the friction coefficient from the compliance hysteresis, as illustrated in Figs. 2 and 7. Having this quantity, since residual stress effects are absent in most instances, the energy release rate can be determined from the critical loads and the specimen dimensions, using eqn. (6).

The general applicability of the method for evaluating the friction coefficient and then obtaining $\mathcal{G}_c$ was rigorously assessed using data obtained on an Al/PMMA system (Fig. 14). For this bimaterial system ($E_2/E_1 \approx 25$), the critical propagation load increased with increase in crack length (Fig. 14), because $\mathcal{G}$ systematically diminishes as the crack extends (see Fig. 6), and because loading generates a range of frictional tractions (Table 10). Applying eqn. (6) and using the measuring friction coefficients (Table 10), the corrected crack propagation load that governs the energy release rate (Fig. 14) exhibits the constancy expected when a critical energy release rate governs fracture such

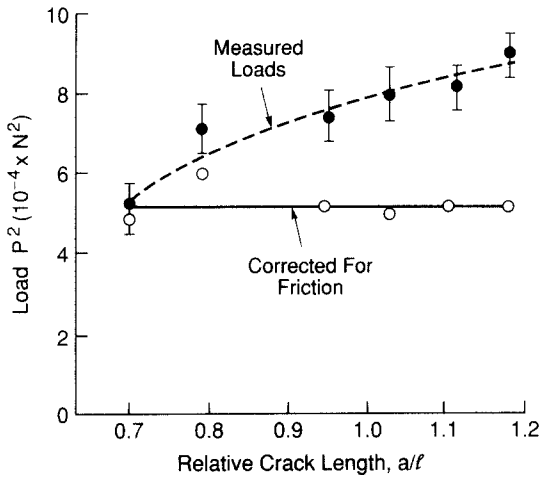


Fig. 14. Trend in crack propagation load $P^2$ in the constant moment region with crack length. Also shown is the value that governs $\mathcal{G}_c$ corrected for friction.

that $\mathcal{G}_c = 6\ \mathrm{Jm}^{-2}$. This value obtains at a nominal phase angle $\Psi = 68°$. Furthermore, results obtained for each of the material systems listed in Table 9 gave specimen independent values of $\mathcal{G}_c$ for the interface, provided that the phase angle $\Psi$ was maintained at the same level. However, it is recognized that changes in $\Psi$ usually cause $\mathcal{G}_c$ to vary (Cao 1988; Cao and Evans, 1989; Evans and Hutchinson, 1989).

The results obtained for the phase angle are dimension sensitive, as discussed by Rice (1988). The choice of length unit used to present the data is not important, provided that the choice is consistent. However, it is noted that the choice can greatly affect the *range* of phase angle applicable to a particular bimaterial interface. For ease of correlation with results obtained for homogeneous systems, for which $\pi/2 < \Psi < \pi/2$, length units that allow $\Psi$ to be primarily within this angular range have been selected. Micrometers appear to be an appropriate choice for systems of present interest and this unit has been used in Table 9. It is also noted that, for the present test specimen having a thin interlayer, the phase angle is modified by the presence of that layer in accordance with (Suo and Hutchinson, 1989)

$$\Psi_{tip} = \Psi + \omega - \epsilon \ln H \tag{16}$$

where $\Psi_{tip}$ refers to the modified value, $H$ is the layer thickness, $\epsilon$ (eqn. 2) refers to the materials on either side of the crack and $\omega$ is an angle (Suo and Hutchinson, 1989) also determined by the materials adjoining the fracture interface. Values of $\Psi_{tip}$ are presented in Table 9 and should be used as the appropriate phase angle for presenting the trends in $\mathcal{G}_c$.

The effect of residual stress on the interpretation of crack propagation measurements is illustrated for the Al/glass system. Calculation of $\mathcal{G}_c$ by neglecting the residual stress, using (6), indicates erroneously that the fracture resistance of the interface is 7 $\mathrm{Jm}^{-2}$ for $\Psi_{tip} = 53°$. The sign of the mismatch stress $\sigma^R$ in this case is negative: the notch being in the glass layer. Consequently, the residual stress initially diminishes $\mathcal{G}$, compared with the value deduced solely from the applied loads, as evident from Fig. 12. The corrected interface toughness obtained using (14) with $\sigma^R = 10$ MPa is $\mathcal{G}_c = 2\ \mathrm{Jm}^{-2}$. It is evident that the residual stress, although small, still has an important influence on the value of $\mathcal{G}_c$ inferred from the measured crack propagation loads.

Table 10
Friction results for Al/PMMA

| Crack length ($a/l$) | Load (N) | Friction coefficient |
|---|---|---|
| 0.7 | 210 | 0.09 |
| 0.8 | 260 | 0.12 |
| 0.95 | 265 | 0.15 |
| 1.0 | 280 | 0.17 |
| 1.1 | 290 | 0.20 |
| 1.2 | 300 | 0.22 |

## 6. Concluding remarks

The mixed mode strain energy release rate for bimaterial flexural specimens has been shown to be influenced both by friction at the loading points and by residual stress. Analyses of these effects in conjunction with experimental measurements have allowed determinations of the critical energy release rate, $\mathcal{G}_c$, for a variety of bimaterial systems. It has also been demonstrated that neglect of

friction and of residual stress would result in erroneous, non-unique values of $\mathcal{G}_c$.

Most other test specimens used for determining $\mathcal{G}_c$ are also subject to the influence of loading point friction and residual stresses. It is thus apparent that specimens which probe other regions of $\mathcal{G}_c$ ($\Psi_{tip}$) space will require a similar analysis, coupled with experimental validation.

## References


Cao, H.C. (1988), Mechanical aspects of interfaces in high performance composites, Ph.D. Thesis, U.C. Berkeley.

Cao, H.C. and A.G. Evans (1989), Mechanical aspects of interfaces in high performance composites, *Mech. of Mater.*, to appear.

Charalambides, P.G. and A.G. Evans (1989), Debonding properties of residually stressed brittle Matrix Composites", *J. Amer. Ceram. Soc. 72[5]*, 746–753.

Charalambides, P.G., J. Lund, A.G. Evans and R.M. McMeeking (1989), A test specimen for determining fracture resistance of bimaterial interfaces, *J. Appl. Mech. 56*, 77–82.

Drory, M.D., M.D. Thouless and A.G. Evans (1989), On the decohesion of thin films, *Acta Metall. 36*, 2019–2028.

Dundurs, J. (1968), Discussion, *J. Appl. Mech. 36, Trans. ASME 91 Ser. E*, 650–652.

Evans, A.G. and J.W. Hutchinson (1989), Effects of non-planarity on the mixed mode fracture resistance of bimaterial interfaces, *Acta Metall. 37*, 909–916.

Lund, J. (1988), The fracture toughness of bimaterial interfaces, M.S. Thesis, UCSB.

Matos, P.P.L., R.M. McMeeking, P.G. Charalambides and M.D. Drory (1989), A method for calculating stress intensities in bimaterial fracture, *Int. J. Fract., 40*, 235–254.

Reimanis, I., V. Jayaram and A.G. Evans (1989), to be published.

Rice, J.R. (1988), Elastic fracture mechanics for interfacial cracks, *J. Appl. Mech. 55*, 98.

Suo, Z. and J.W. Hutchinson (1989), Santwich test specimens for measuring interface crack toughness, *Mater. Sci. Eng. A107*, 135–143.